ADVANCED FUNCTIONAL MATERIALS
www.afm-journal.de

Bioinspired Hierarchical Hydrogels Engineered with Extreme Impact Resistance

*Yun Tan, Yafei Wang, Pei Zhang, Jun Li, Fucheng Wang, Liangjie Shan, Jin Guo, Zongbao Wang, and Ji Liu**

The development of extreme impact-resistant materials holds significant importance across engineering applications, yet remains constrained by the inherent trade-offs among mechanical strength, toughness, and energy dissipation efficiency. Drawing inspiration from natural models, particularly the unique structural design and toughening mechanisms of the mantis shrimp's dactyl club, a kind of nanocomposite hydrogel is developed by synergistically integrating polymer elastic microspheres with enzyme-induced biomineralization. This bioinspired approach produces microsphere-reinforced nanocomposite hydrogels (MNHs) that concurrently deliver exceptional strength, remarkable fracture toughness, and unprecedented resistance to ballistic impacts, surpassing the performance of all existing high-strength hydrogels, thus underscoring their potential for protective applications. Nonlinear numerical and theoretical analyses elucidate the dynamic fracture mechanisms governing both quasi-static and high-speed impact scenarios, revealing crack deflection, microcrack nucleation, and energy redistribution as key toughening pathways. This work not only advances the fundamental understanding of bioinspired structural design principles but also establishes a universal blueprint for next-generation impact-resistant materials, unlocking new frontiers for polymer composites in mechanically demanding scenarios.

1. Introduction

Impact-resistant materials play a pivotal role in safeguarding biological tissues, functional devices, and engineered systems against high-velocity threats, including projectiles and shockwaves.[1–3] Natural systems, such as bamboo,[4,5] nacre,[6,7] and other marine organisms,[8] have emerged as unparalleled sources of inspiration for designing advanced materials with outstanding mechanical performance. The mantis shrimp's dactyl club, for instance, employs a multiscale hierarchical architecture combining mineralized layers and organic components to dissipate energy, resist catastrophic fracture, and endure repetitive high-impact strikes—a feat critical for breaking hard-shelled prey (**Figure 1a**).[8,9] The dactyl club exhibits a sophisticated multi-layered architecture, with each structural layer contributing distinctively to impact resistance: 1) the outer impact region is composed of highly mineralized chitin fibrils arranged; 2) the intermediate periodic region contains elastic biopolymers for providing elastic energy storage or energy dissipation; 3) the inner core features a dense, mineralized structure that absorbs compressive forces. Recent advances in impact-resistant materials have focused on biomimetic strategies, such as polymeric elastomers,[10–12] hierarchical gels,[2,13–16] and organic/inorganic nanocomposites,[17–20] aiming to replicate the energy dissipation mechanisms observed in natural systems. These materials typically attenuate impact damage through deformation-driven energy absorption, bond rupture, and interlayer friction.[2,17,21,22] Nevertheless, reconciling extreme impact resistance (e.g., ballistic threats) with high toughness remains a formidable challenge, particularly for defense applications.[13,23] Extreme impact resistance prioritizes immediate energy dissipation via rigid/frangible structures (e.g., ceramic layers in armor), which limits ductility and fracture toughness. Engineered hydrogels with bioinspired hierarchical structures have shown exceptional promise in this regard, achieving unprecedented combinations of strength, modulus, and toughness.[14,24–28] Notable examples include nacre-mimetic hydrogels and high-mineral-content composites (>70 wt.% inorganic phase), where aligned micro/nanoparticles within a polymer matrix facilitate simultaneous achievement of high rigidity and efficient energy dissipation.[20,26,29,30] However, limitations in material compatibility, scalability, and inorganic loading often restrict mechanical performance, resulting in hydrogels with inferior impact resistance.[14,31]

Y. Tan, Y. Wang, P. Zhang, J. Li, F. Wang, L. Shan, J. Liu
Department of Mechanical and Energy Engineering
Southern University of Science and Technology
Shenzhen 518055, China
E-mail: liuj9@sustech.edu.cn
J. Guo, Z. Wang
School of Materials Science and Chemical Engineering
Ningbo University
Ningbo 315211, China

The ORCID identification number(s) for the author(s) of this article can be found under https://doi.org/10.1002/adfm.202508034

DOI: 10.1002/adfm.202508034

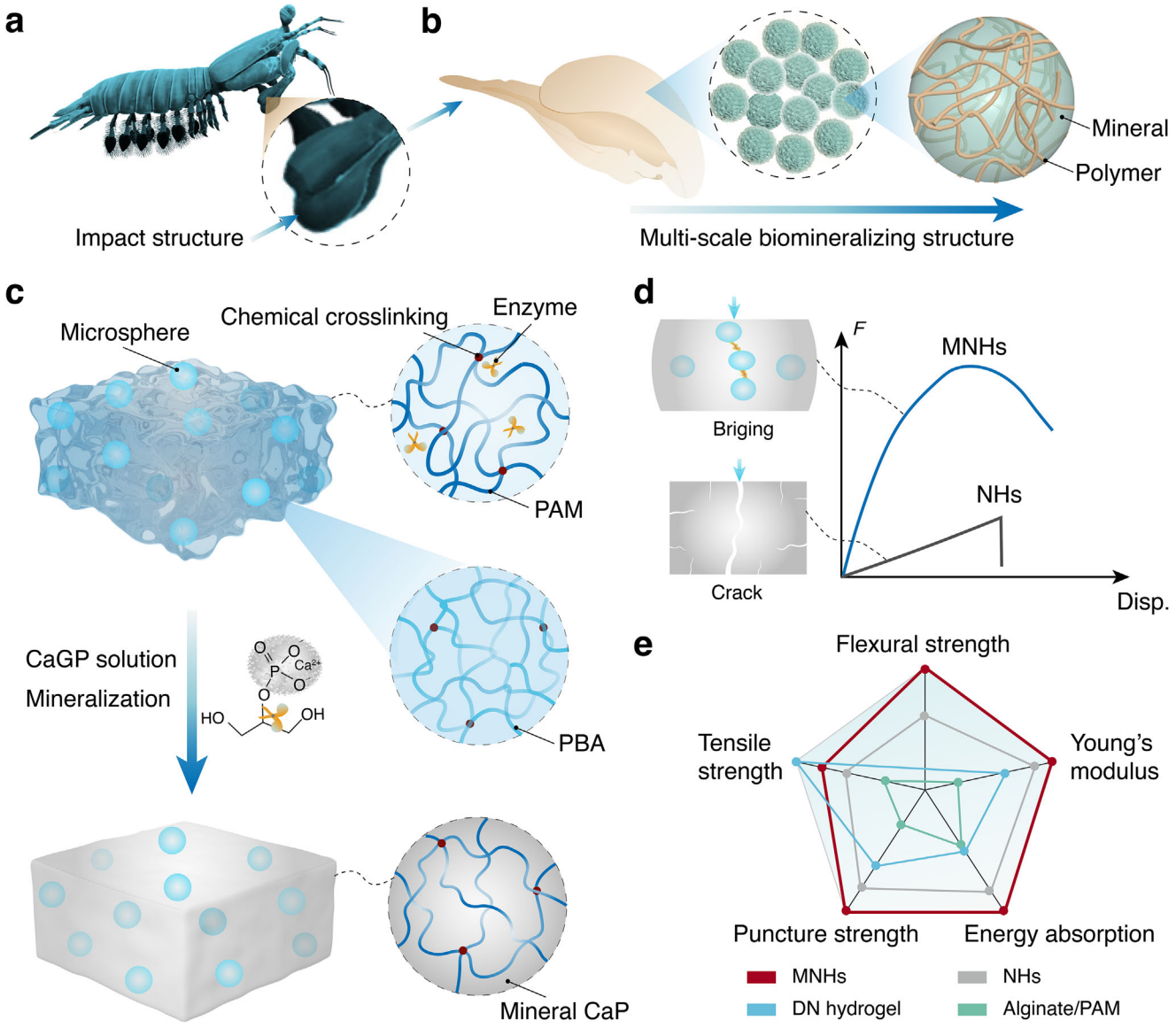

Figure 1. Bioinspired design and fabrication of nanocomposite hydrogel materials through enzyme-mediated biomineralization. a, b) Schematic diagram of the mantis shrimp's dactyl club and its multiscale hierarchical structures. c) Schematic illustration for constructing the nanocomposite hydrogel materials, by integrating elastic microspheres and inorganic nanoparticles through enzyme-mediated mineralization. d) Representative force-displacement curves and energy dissipation mechanism for the nanocomposite hydrogel materials with or without elastic microspheres. e) A radar map comparing the mechanical parameters, including puncture strength, flexural strength, tensile strength, Young's modulus, and energy absorption, of various hydrogels, including our microsphere-reinforced nanocomposite hydrogels (MNHs), Alginate/PAM tough hydrogel,[25] double network (DN) hydrogel,[35] and nanocomposite hydrogels (NHs) through biomineralization.[26] Part of the data is adapted from previously reported literatures,[24,25,33] and summarized in Table S1 (Supporting Information).

In this work, we present a kind of microsphere-reinforced nanocomposite hydrogels (MNHs), engineered through a multiscale hierarchical toughening strategy as inspired by the mantis shrimp's biomineralization process (Figure 1a,b). On one hand, integrating uniformly dispersed poly(n-butyl acrylate) (PBA) elastic microspheres into an enzymatically mineralized hydrogel matrix achieves energy storage, dissipation, and stress redistribution through the elastic microspheres deform, leading to the reversible and irreversible deformation or damage of microspheres.[32–34] On the other hand, the rigid high mineralized phase content ($Ca_3(PO_4)_2$) grown in situ within the hydrogel matrix is able to arrest crack propagation (Figure 1c). Unlike brittle mineralized hydrogels, the MNHs preserve intrinsic strength and hardness while enhancing modulus and toughness, enabling exceptional quasi-static puncture resistance and dynamic ballistic protection (Figure 1d).[26,32] The mechanical properties of MNHs are tunable through microsphere size and volume fraction adjustments, meeting extreme demands in complex environments—from static bending to high-velocity impact scenarios. As a proof of concept, our mineralized hydrogel

demonstrates superior ballistic resistance compared to state-of-the-art high-strength hydrogels, addressing the classical inherent trade-offs among mechanical strength, toughness, and energy dissipation efficiency. This breakthrough significantly advances the development of polymer composites for extreme mechanical environments.

2. Results and Discussion

2.1. MNHs Fabricated through Enzyme-Induced Mineralization

Inspired by the natural prototypes and biomineralization process,[8,29] here we developed a microsphere-reinforced nanocomposite hydrogels (MNHs) through an enzyme-mediated in situ mineralization strategy (Figure 1). This system integrates poly(n-butyl acrylate) elastic microspheres (PBA, ≈150 nm diameter; Figures S1 and S2, Supporting Information) within a chemically-crosslinked polyacrylamide (PAM) hydrogel network.[33] Key components include acrylamide monomers for polymeric network construction and alkaline phosphatase (ALP) as the biomineralization catalyst, assembled via photopolymerization to form the microsphere-composite hydrogel. Subsequent 7-day biomineralization within a calcium glycerophosphate solution (CaGP, 11 wt.%) induced the formation of amorphous calcium phosphate ($Ca_3(PO_4)_2$) nanoparticles, yielding the final MNHs architectures (Figure 1c). The exceptional energy dissipation capacity stems from two synergistic mechanisms: elastic deformation of PBA microspheres and dynamic interactions among the organic and mineral phases (Figure 1d). The elastic microspheres embedded in the nanocomposite hydrogels (MNHs) induce non-linear crack propagation and complex fracture surfaces through interfacial debonding, polymer chain friction, and chemical bond rupture. These synergistic mechanisms generate tortuous fracture paths characterized by crack branching, multiplication, and deflection/twisting. Crucially, these processes substantially enhance the energy dissipation capacity of MNHs. This performance surpasses conventional high-strength hydrogels through multidimensional mechanical optimization,[25,26,35] achieving unprecedented synergy between puncture resistance, flexural strength, and dynamic impact absorption (Figure 1e; Table S1, Supporting Information).

The PAM polymer network serves as a mechanical confinement template for alkaline phosphatase (ALP), effectively limiting the enzyme diffusion into the CaGP solution during mineralization (Figures S3 and S4, Supporting Information). Subsequent in situ biomimetic mineralization yielded amorphous calcium phosphate ($Ca_3(PO_4)_2$) nanoparticles uniformly distributed throughout the hydrogel network.[29] By modulating polymer chain-ALP affinity, we achieved precise control over mineralization kinetics and particle dimensions (Figure S5, Supporting Information). After 7-day soaking within the CaGP solution, the MNHs reached comparable biomineralization efficacy to the analogue in the absence of microspheres (≈40 wt.% mass fraction, Figure S6, Supporting Information),[26] while exhibiting enhanced structural organization (**Figure 2**b; Figure S7, Supporting Information). The hierarchical micro/nano composite network facilitated the formation of uniform elastic microspheres coupled with finer amorphous $Ca_3(PO_4)_2$ nanostructures (50–100 nm in diameter). Mineral volume fraction progressively increased with the incubation time, reaching optimal values of 20 vol% (corresponding to ≈42 wt.% mass fraction) at Day 7, demonstrating that microsphere incorporation does not compromise network mineralization capacity. Nanoindentation analysis revealed significant mechanical enhancement in MNHs compared to the nanocomposite hydrogels without microspheres (NHs, Figure 2c). It exhibited a six-fold increase in hardness and an eight-fold elevation in reduced modulus (Figure 2d), consistent with previous reports of mechanically reinforced organic/inorganic nanocomposite materials.[36,37] This performance improvement correlates with the development of a homogeneous, densely mineralized nanostructure during the biomineralization process.

2.2. Mechanical Toughening Mechanism of the MNHs

To systematically evaluate the contribution of MNHs microspheres to mechanical property enhancement, we conducted tensile tests on these MNHs materials. The enzyme-induced mineralization process significantly improved the mechanical performance, with tensile strength increasing by 2–3 orders of magnitude and Young's modulus by 3–4 orders of magnitude compared to non-mineralized hydrogels (**Figure 3**a). This mechanical enhancement is consistent with the mechanism proposed by Tiller et al.[26] wherein permeable nanostructures formed during mineralization govern the mechanical reinforcement. Notably, the incorporation of elastic microspheres further amplified these effects. Prior to mineralization, the microsphere-PAM hydrogels (MHs) exhibited a tensile strength of 30 kPa (3× higher than pure PAM hydrogel) and a Young's modulus of 50 kPa (2× higher than pure PAM hydrogel). Following a 7-day mineralization, MNHs achieved remarkable mechanical properties: 3.3 MPa tensile strength and 120 MPa Young's modulus (Figure 3b), representing 6-fold and 4-fold improvements over the NHs, respectively. Additionally, MNHs demonstrated a 9-fold increase in fracture toughness compared to NHs (Figure S8, Supporting Information). These results suggest that PBA microspheres could effectively enhance the mechanical properties through mechanisms beyond conventional organic/inorganic nanocomposite effects. Specifically, microsphere incorporation promotes interfacial interactions between organic and inorganic phases, improves structural homogeneity, reduces densification, and mitigates defect formation. Crucially, MNHs outperforms both state-of-the-art high-strength/toughness hydrogels[25–27,35,38,39] and naturally mineralized tissues[40,41] in terms of mechanical strength and modulus (Figure 3c). This work establishes a viable strategy for resolving the strength-toughness trade-off in hydrogel materials through elastic microsphere-reinforced organic/inorganic nanocomposites,[42] as demonstrated by our MNHs system.

To elucidate the mechanistic foundations of strengthening and toughening in the MNHs material system, we performed comprehensive micromechanical analyses coupled with nonlinear finite element modeling (FEM). A 2D representative volume element (RVE) model was systematically constructed through customized Python programming, incorporating elastic microspheres with volume fractions ranging from 0% to 25%. The fracture evolution of microspheres was investigated using a Rankine criterion, where exceeding the critical tensile stress triggered

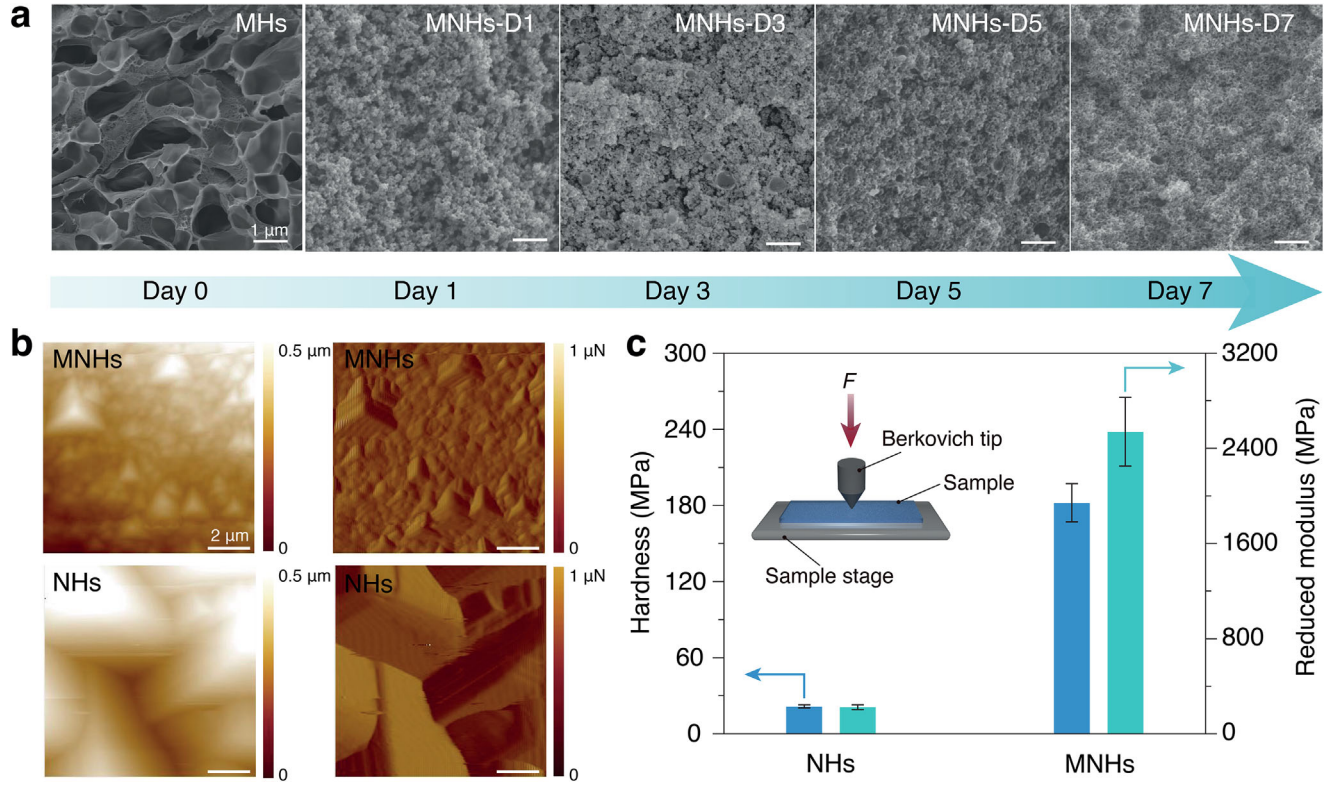

Figure 2. Structure and composition analysis of the MNHs during the enzyme-mediated biomineralization. a) Evolution of the microstructures of the MNHs during a 7-day mineralization process. b) Surface morphology of various hydrogel materials through nanoindentation tests. c) Summary of the mechanical parameters (hardness and reduced modulus) Hydrogel materials, including MNHs and NHs, were tested. Scale bar: 2 μm. Data in (c) are presented as means ± S.D., $n = 3$.

sequential Mode I (tensile softening) and Mode II (shear softening) fracture mechanisms. For the mineralized matrix, a ductile fracture criterion was employed, with damage evolution characterized through experimental true stress-strain data and linearized displacement-based failure criteria. Comparative analysis of stress-strain curves revealed that MNHs containing 15 vol% microspheres demonstrated 23.7% greater ultimate tensile strength and 41.2% enhanced fracture strain, in comparison to microsphere-free controls. Fractographic examination showed that geometric mismatch between size-dependent microspheres and the matrix induces interfacial crack initiation, followed by progressive shear/ductile fracture modes, contrasting with the smooth fracture interface observed in pure matrix specimens.

Through parametric investigation of microsphere dimensions and spatial distributions (Figure S9, Supporting Information), strength (Figure 3e) and toughness (Figure 3f) phase diagrams were established. Mixture theory-based modeling incorporating microsphere interactions revealed that optimal mechanical properties cluster in the upper-right quadrant of these diagrams, indicating that microsphere geometric effects and stochastic distribution patterns govern damage evolution kinetics, fracture resistance mechanisms, crack propagation trajectories, and final fracture morphology. Notably, reduced microsphere diameter ($D < 50$ μm) enhanced fracture toughness through intensified cluster effects, while increased volume fraction ($\varphi > 20$ vol%) introduced nonlinear complexity from particle clustering. Deformation-failure progression analysis revealed four distinct regimes: Stage I (1% strain) exhibited interfacial stress concentration with microsphere-dominated energy dissipation; Stage II (2% strain) showed geometric mismatch-induced stress localization and cluster-chain formation; Stage III (3%–4% strain) demonstrated stress flux redistribution through microsphere clusters; and Stage IV (>5% strain) displayed synergistic fracture mechanisms combining bridging effects, shear band formation, and tortuous crack propagation (Figure 3g–k).[43] This multiscale coupling of geometric mismatch, size-dependent cluster behavior, and stochastic distribution effects increases fracture work by 2.8–3.5 times compared to the homogeneous matrices, fundamentally explaining the superior mechanical performance of MNHs systems.

To elucidate the contribution of elastic microspheres to the mechanical reinforcement of mineralized hydrogels, we conducted three-point bending tests to evaluate their uniaxial stress characteristics (**Figure 4a**). The MNHs composites demonstrated remarkable mechanical enhancement, with peak forces of 0.9 and 1.7 N at 15 and 20 vol% microsphere volume fractions, respectively, significantly surpassing the 0.1 N observed in microsphere-free controls. This force elevation exhibited clear microsphere concentration dependence while maintaining constant mineralized component volume fractions (≈20 vol%). Fractographic analysis revealed distinct failure modes: MNHs specimens displayed zigzag ductile fractures compared to the

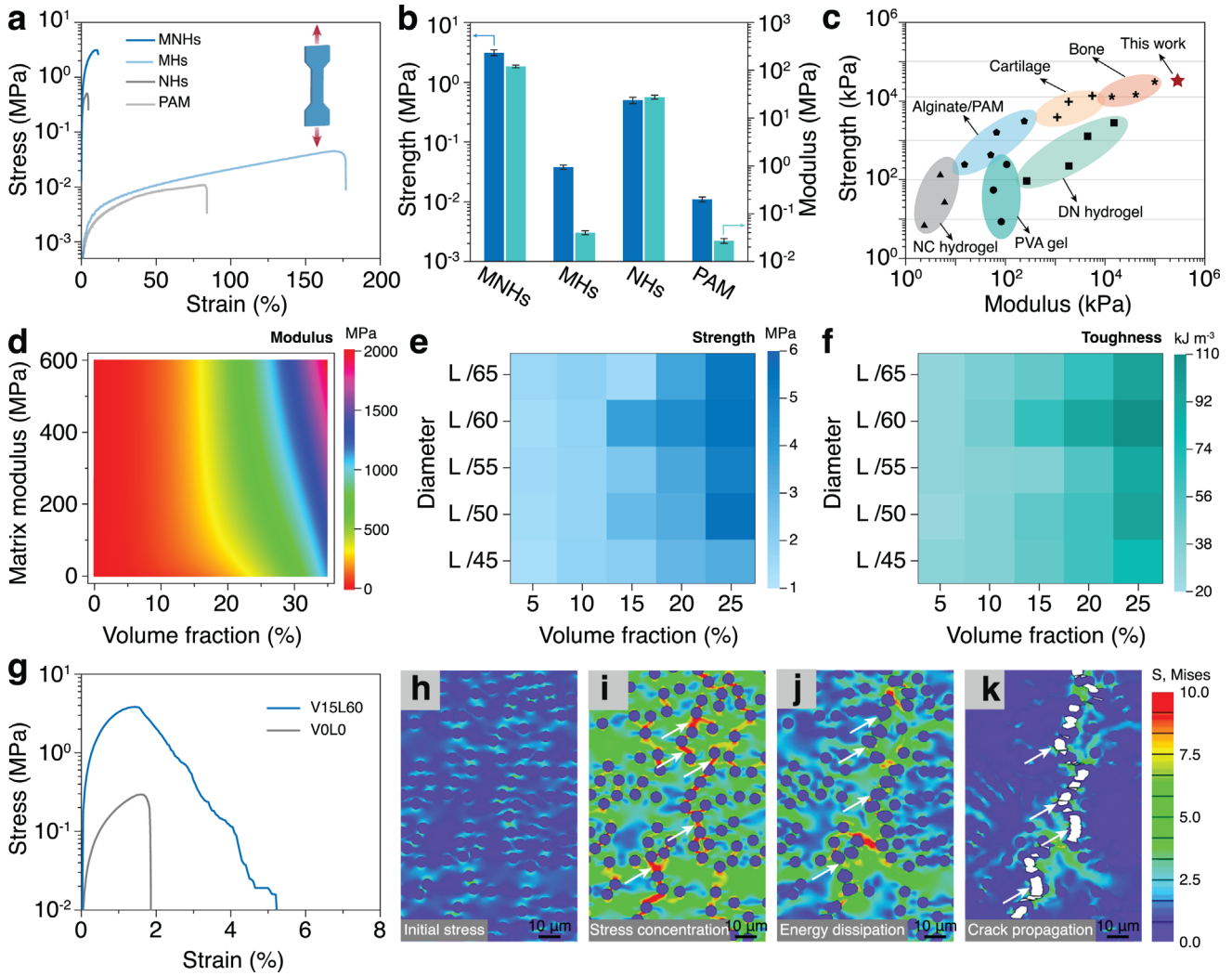

Figure 3. Mechanical properties and finite element modeling (FEM) analysis of the MNHs. a) Representative tensile test curves for various hydrogel materials, including MNHs, MHs, NHs, and PAM hydrogels. b) Summary of tensile strength and Young's modulus of these hydrogel materials. c) Comparison chart by plotting the strength and Young's modulus of various synthetic hydrogel materials and biological tissues (i.e., cartilages and bones) Most of the data points are adapted from previous literature.[25–27,35,38,41] d) Simulated coupling effect of matrix modulus and microsphere volume fraction according to the mechanical response of the MNHs. e, f) Phase diagram for the plotting of strength (e) and toughness (f) with various volume fractions and dimensions of elastic microspheres within the nanocomposite hydrogel materials. g) Representative stress-strain responses of the nanocomposite hydrogel materials with (15% volume fraction) or without elastic microspheres. (The notation 'VxLy' indicates that the nanocomposite hydrogel materials have an x (%) volume fraction, and the edge length of the representative volume element in the nonlinear finite element simulation is 1/y of the sample edge length) h–k) Deformation-failure-fracture evolution process for nanocomposite hydrogel materials, with a volume fraction of 15% for elastic microspheres. Data in (b) are presented as means ± S.D., $n = 3$.

brittle fracture characteristic of NHs controls,[42,43] suggesting improved energy dissipation mechanisms. Quantitative mechanical characterization showed substantial improvements in flexural properties (Figure 4b). The MNHs composites achieved flexural strength >13.5 MPa and stiffness >1.8 GPa, representing 4.5× and 3.6× enhancements over NHs values (3.0 MPa, 0.5 GPa), respectively. These enhancements originate from three synergistic mechanisms: optimized composite architecture integrating microspheres with mineral phases, robust interfacial interactions, and energy dissipation through microsphere deformation. Toughness evaluation following ASTM C1018 standards revealed multi-level toughness indices for MNHs (I_5 = 5.2, I_{10} = 15.0, I_{20} = 35.0), contrasting with the single-index brittle failure (I_5 = 7.5) observed in NHs (Figure 4c).[44] This multi-stage toughening behavior indicates progressive energy absorption capabilities in the microsphere-reinforced system.

To validate the universality of this reinforcement strategy, we implemented two distinct microsphere types: elastic PAM and rigid SiO_2 microspheres (Figures S10–S12, Supporting Information).[34,45] Both systems showed significant peak force improvements over NHs controls. Notably, PAM-MNHs exhibited characteristic toughness indices (I_5 = 8.1, I_{10} = 10.0), while SiO_2-MNHs demonstrated strength enhancement without toughness improvement (Figure 4e,f). While

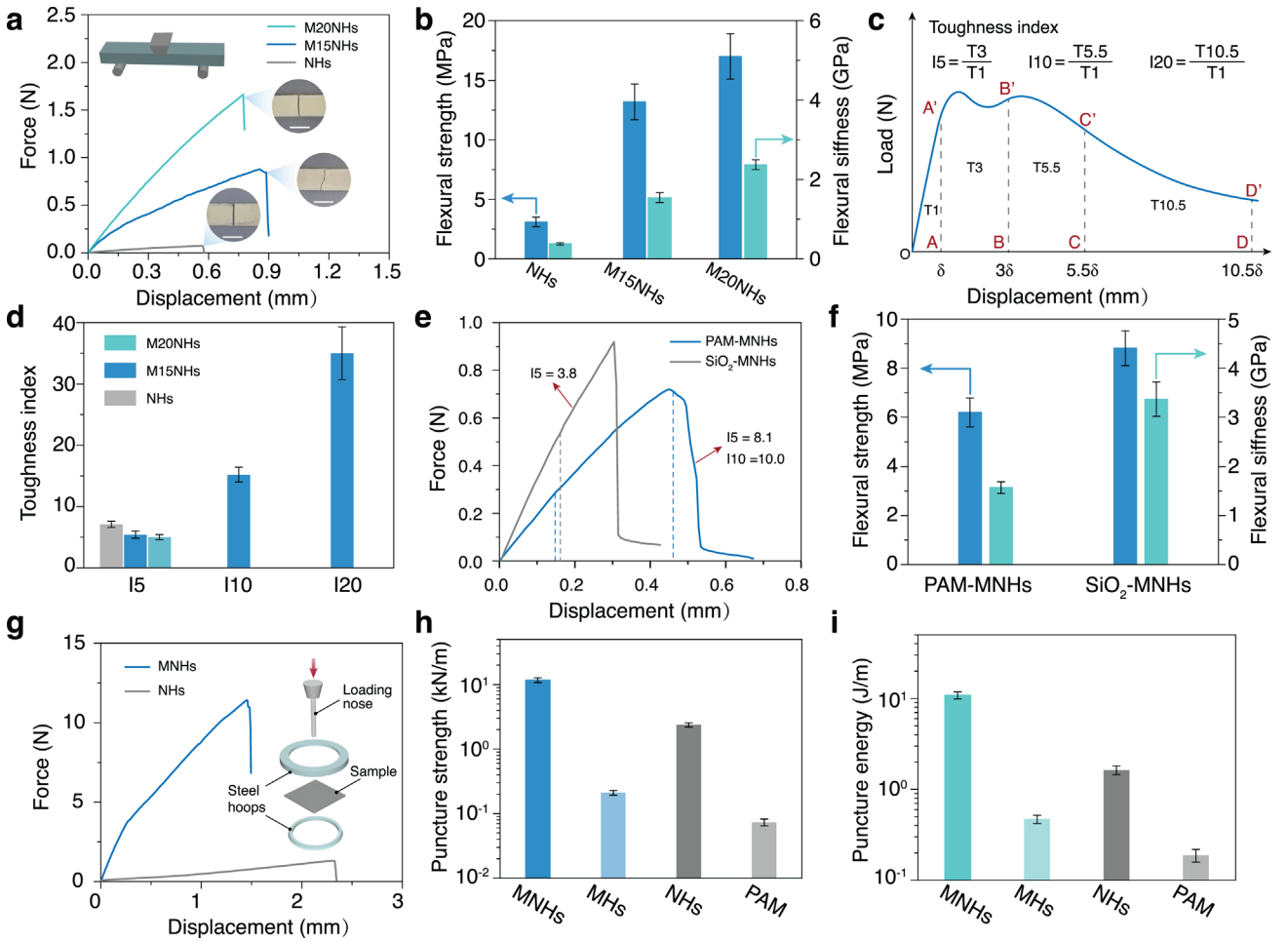

Figure 4. Mechanical bending resistance and quasi-static puncture properties of the MNHs. a) Representative three-point bending test curves for the MNHs. MxNHs represents the volume fraction of the microspheres in the MNHs sample as x. Without special notes, the volume fraction of microspheres in MNHs is 15 vol%. b) Summary of flexural strength and flexural stiffness for these hydrogel materials through the three-point bending tests. c) Schematic diagram for quantifying the bending toughness index (I_5, I_{10}, and I_{20}) following the American Society of Testing Materials standard (ASTM C1018). d) Summary of the bending toughness index for various hydrogel materials. e) Three-point bending test curves for nanocomposite hydrogel materials with PAM microsphere (≈20 μm) or silica nanoparticles (100–150 nm). f) Summary of the flexural strength and flexural stiffness of the nanocomposite hydrogel materials filled with either PAM microsphere or silica nanoparticles. g) Representative plotting of the puncture force against loading nose displacement for the nanocomposite hydrogel materials. h,i) Summary of the maximal puncture force (F_{max}, h) and puncture energy (E, i) of various nanocomposite hydrogel materials. Scale bar: 1 cm. Data in (b, d, f, h, i) are presented as means ± S.D., $n = 3$.

polyacrylamide-based elastic microspheres were incorporated into the system, their limited performance enhancement can be attributed to three key factors: 1) The relatively low modulus of polyacrylamide microspheres (typically ≈10 kPa) provides insufficient stress transfer at the polymer-mineral interface, compromising their reinforcing efficiency; 2) Their high water absorption capacity leads to swelling-induced interface weakening and a relatively looser structure in the mineralized hydrogel matrix. This divergence highlights the critical role of elastic microsphere deformation in energy dissipation, as rigid SiO_2 microspheres cannot undergo comparable energy-absorbing deformations. Control experiments confirmed that mineral content variations (Figures S13–S17, Supporting Information) did not account for these performance differences, further supporting the microsphere-mediated enhancement mechanism. These results collectively demonstrate that incorporating elastic microspheres into biomineralized systems creates a universal strategy for simultaneous strength enhancement and toughness improvement through controlled energy dissipation mechanisms.

The quasi-static puncture resistance of MNHs was systematically evaluated at predetermined deformation, demonstrating remarkable mechanical enhancements compared to both conventional NHs and non-mineralized hydrogels (MHs and PAM hydrogels) (Figure 4g). Quantitative analysis demonstrated a maximum puncture force of 12 N, representing a 10× improvement over NHs, accompanied by a puncture strength of 11.7 kN m^{-1} (5-fold increase) and puncture energy of 10.8 J m^{-1} (8-fold enhancement), as detailed in Figure 4h,i and Figure S18 (Supporting Information). Notably, MNHs exhibited 1-2 orders of magnitude superiority in both puncture strength and energy dissipation capacity compared to their non-mineralized counterparts. This performance breakthrough stems from the synergistic

interaction of two fundamental mechanisms: inorganic minerals providing enhanced resistance to stress concentration, and elastic microsphere-mediated energy dissipation through controlled deformation processes.[46,47]

2.3. Impact Resistance of the MNHs

Low-cost organic/inorganic nanocomposites exhibiting high energy-absorption performance hold significant promise for body armor and engineered soft protective equipment.[2,13] To evaluate the ballistic resistance potential of the nanocomposite hydrogel materials, comparative impact tests were conducted using water projectiles (5.8 m s^{-1}, 0.32 g) and steel bullets (200 m s^{-1}, 0.2 g) on various hydrogel materials (**Figure** 5a; Figure S19, Supporting Information). Under a water bomb impact (Movie S3, Supporting Information), the MNHs demonstrated exceptional integrity with neither fracture nor surface crack formation (Figure 5b), while MHs specimens exhibited catastrophic failure at lower impact velocities (Figure 5c). Quantitative evaluation using steel projectiles revealed that MNHs achieved a ballistic energy absorption capacity of 1.5 ± 0.2 kJ m^{-1} (Figure S20, Supporting Information), surpassing MHs, NHs, and PAM by factors of ≈11, 3, and 21, respectively (Figure 5d).

Fractographic analysis revealed distinct failure mechanisms; the MNHs developed irregular jagged notches (Figure 5e–g), contrasting with the circular notches observed in NHs (Figure 5h–j). This disparity originates from MNHs multiscale energy dissipation architecture involving the microsphere elastic deformation, dynamic interfacial bonding interactions among the microspheres, minerals, and polymer network. Benchmarking against reported hydrogel systems confirms MNHs superior combination of strength (3.3 ± 0.3 MPa), toughness (1500 ± 200 J m^{-2}), and ballistic performance (Figure 5k; Figure S21 and Movie S4, Supporting Information).[2,20,25,29,35] These findings establish MNHs as a paradigm-shifting material platform for impact-resistant applications through synergistic hierarchical energy dissipation. Based on the low cost, excellent impact resistance, and simple portability of MNHs, they can be easily integrated with multifunctional features such as flexible sensing and thermal management. This provides crucial support for developing new types of armored materials that combine military-grade protection with capabilities like information transmission and energy management.

To elucidate the energy dissipation mechanisms of our MNHs, we classify the impacting process into two categories.[48,49] The first category involves elastic impact, where, theoretically, a rigid spherical projectile does not need to penetrate the plate. The second category pertains to elastoplastic impact, in which the rigid spherical projectile can penetrate the plate. We begin by examining the first category. Drawing on Zener's composite material plate model[50] for a deep impact with high velocity, the governing equation for elastic impact is expressed as follows:

$$\frac{d^2\bar{\Delta}}{d\bar{t}^2} + 2\lambda\bar{\Delta}\frac{d\bar{\Delta}}{d\bar{t}} + \left(\bar{\Delta}\right)^2 = 0 \tag{1}$$

where $\bar{\Delta}|_{\bar{t}=0} = 0$, $\frac{d\bar{\Delta}}{d\bar{t}}|_{\bar{t}=0} = 1$, $\bar{\Delta}$ denotes the dimensionless impact depth, $\bar{t}$ represents the dimensionless time, and $\bar{\lambda}$ is the dimensionless energy dissipation factor (e.g., energy loss caused by internal material friction, air resistance, and acoustic radiation), which is related to the maximum impact depth $\bar{\Delta}_{max}$ by the following equation:

$$\bar{\Delta}_{max} = \left(\lambda + 1.5^{-2/3}\right)^{-1/2} \tag{2}$$

With respect to the governing equation Equation (1), a closed-form solution has been derived in previous studies using Homotopy analysis.[51] In this work, we provide its simplest approximate solution, which facilitates a deeper understanding of the energy dissipation mechanisms, that is:

$$\bar{\Delta} \approx \frac{e^{-1/2(\lambda-0.125)\bar{\Delta}_{max}\bar{t}}}{\omega}\sin\omega\bar{t},\ with\ \omega = \frac{1}{2}\left(3.2\bar{\Delta}_{max} - (\lambda-0.125)^2\bar{\Delta}_{max}^2\right)^{\frac{1}{2}} \tag{3}$$

As shown in Figure 5l, based on the analytical solution (see Equation 3), we plotted the distribution of the energy dissipation factor $\bar{\lambda}$ and dimensionless time $\bar{t}$ with respect to the dimensionless contact depth $\bar{\Delta}$ in the first scenario. It is evident that as the volume fraction of the gel microspheres increases, their density (ratio $\rho_{sphere}/\rho_{matrix}$) also increases, leading to a higher dimensionless energy dissipation factor $\bar{\lambda} \sim \left(\rho_{sphere}/\rho_{matrix}\right)^{2/3}$ in the system.[48,51] This, in turn, results in a reduction in the contact depth $\bar{\Delta}$, indicating a significant energy absorption effect of the enzyme-induced biomineralized hydrogel plate on the steel ball.

Nonlinear finite element analysis (FEA) using ABAQUS was employed to examine stress wave propagation dynamics and fracture behavior in nanocomposite hydrogel plates (20% mineral volume fraction) during high-velocity steel sphere penetration.[51,52] As visualized in Figure 5m and Movie S5 (Supporting Information), impact-initiated stress waves radiate radially from the contact point, exhibiting tortuous propagation paths attributed to energy dissipation through elastic microsphere deformation. This contrasts sharply with control systems in the absence of elastic microspheres (Figure 5n; Movie S6, Supporting Information), where smoother wave fronts correlate with 7.1% faster projectile penetration (18 m s^{-1} vs 17 m s^{-1} in microsphere-containing systems at 20 m s^{-1} initial velocity, Figure S22, Supporting Information). Post-impact analysis reveals critical rebound phenomena at plate boundaries, with stress wave reflections concentrating energy near the material center. The synergistic integration of microsphere-mediated energy dissipation (38% impact energy attenuation) and mineralization-derived strength (13.5 MPa compressive resistance) demonstrates the viability of engineering organic/inorganic nanocomposites combining fracture toughness (1500 J m^{-2}) with ballistic resistance, a critical advancement for military-grade protective materials and energy-absorbing engineering structures.

3. Conclusion

Inspired by the structural principles and toughening mechanisms observed in natural systems—particularly the dactyl club of the mantis shrimp, we develop a straightforward yet effective design strategy employing the enzyme-induced in situ mineralization to fabricate the microsphere-reinforced nanocomposite hydrogels (MNHs). This bioinspired system achieves

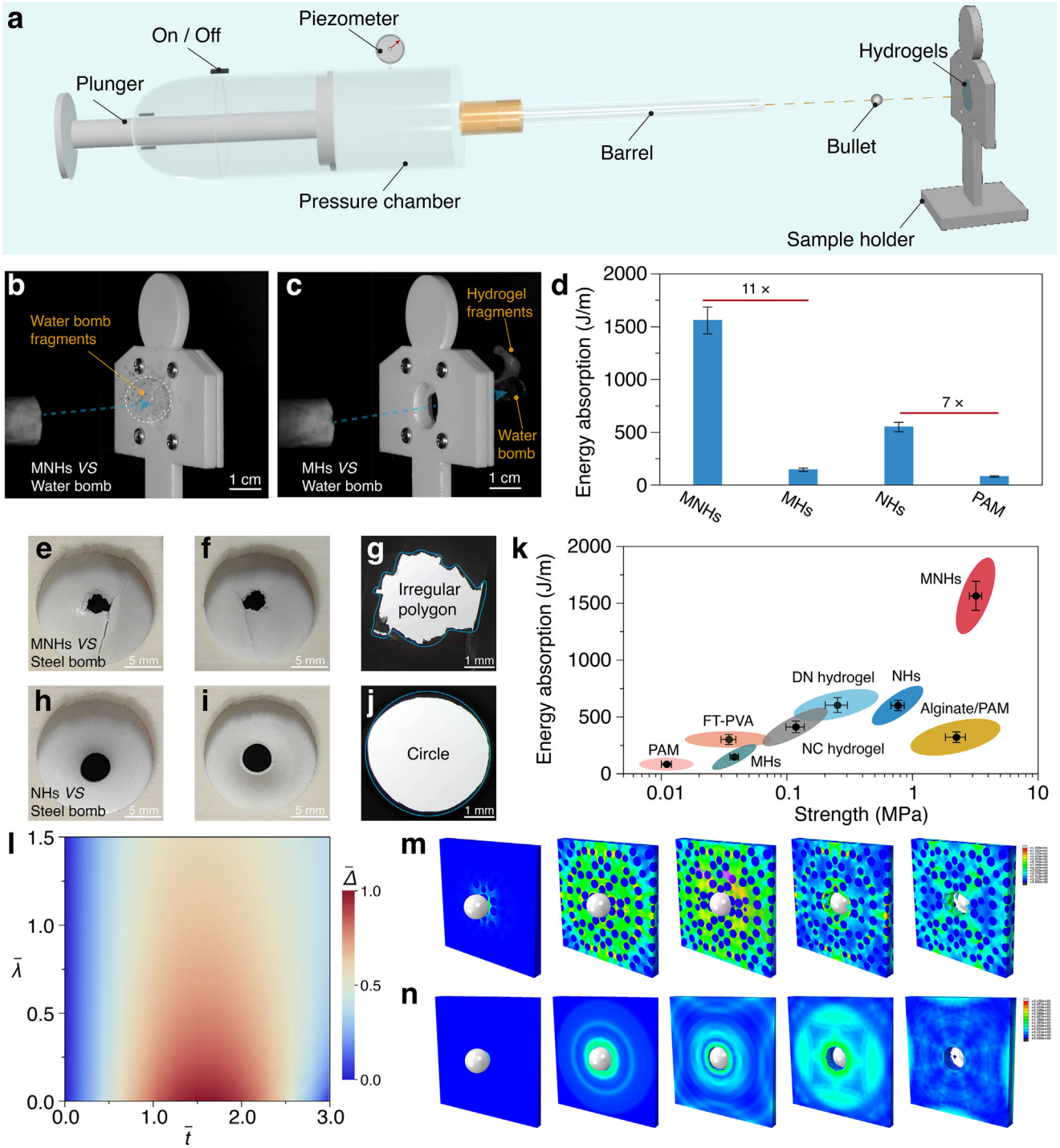

Figure 5. Impact resistance of the MNHs. a) Schematic diagram for a high-speed bullet impacting a hydrogel sample. b) Summary of ballistic energy absorption for various hydrogel materials, including MNHs, NHs, MHs, and PAM hydrogels. c,d) High-speed snapshot image recording the moment when a high-speed bomb penetrates the hydrogel samples, with a steel bomb (0.2 g, 200 m s^{-1}) for the MNHs sample (c), and a water bomb (0.32 g, 5.8 m s^{-1}) for the MHs sample (d). e–j) Optical images (front, e and h; back, f and i), contour photographs (g, j) of the notches in MNHs (top) and NHs (bottom) after being impacted by a steel projectile. k) Comparison chart plotting the ballistic energy absorption versus strength for different hydrogel materials. l) The distribution of the energy dissipation factor $\bar{\lambda}$ and dimensionless time $\bar{t}$ with respect to the dimensionless contact depth $\bar{\Delta}$. The propagation process of stress waves generated at the contact point, when a rigid sphere impacts a nanocomposite hydrogel sample with (m) or without (n) elastic microspheres. ABAQUS simulated the velocity change of the steel bomb before and after impacting the nanocomposite hydrogel samples. Data from other hydrogel materials were adapted from previously reported literature.[2,20,25,29,35] Data in (b) and (k) are presented as means ± S.D., $n = 3$.

remarkable quasi-static mechanical properties and dynamic impact resistance, surpassing conventional tough hydrogels and double-network hydrogels in terms of strength, elastic modulus, and energy dissipation capacity. Finite element simulations and closed-form solutions further elucidate the underlying mechanisms governing fracture behavior under both quasi-static and dynamic conditions, highlighting the synergistic interplay of multiple energy dissipation pathways, including elastic microsphere deformation, dynamic interface among the microspheres, minerals, and the hydrogel network. This work advances fundamental understanding of bioinspired material design while establishing a versatile platform for engineering next-generation protective materials with programmable mechanical performance. The proposed methodology holds significant promise for diverse applications, ranging from impact-resistant protective gear to advanced biomedical engineering solutions.

Supporting Information

Supporting Information is available from the Wiley Online Library or from the author.

Acknowledgements

Y.T. and Y.W. contributed equally to this work. The authors acknowledged the financial support from the National Key R&D Program of China (2024YFA0920100), the National Natural Science Foundation of China (52373139, U2436202, 52403160, and 12202105), Guangdong Basic and Applied Basic Research Foundation (2023A1515110532 and 2024A1515240042), Basic Research Program of Shenzhen (20231116101626002 and JCYJ20240813094159001). The authors also gratefully acknowledge the support from the Shenzhen Science and Technology Innovation Commission (KJZD20240903101400001) and the Development and Reform Commission of Shenzhen Municipality (XMHT20240115003). The authors would like to acknowledge the technical support from SUSTech Core Research Facilities.

Conflict of Interest

The authors declare no conflict of interest.

Data Availability Statement

The data that support the findings of this study are available from the corresponding author upon reasonable request.

Keywords

bioinspired, energy dissipation, hierarchical structure, hydrogels, impact resistance

Received: March 31, 2025
Revised: June 13, 2025
Published online:

[1] C. M. Portela, B. W. Edwards, D. Veysset, Y. Sun, K. A. Nelson, D. M. Kochmann, J. R. Greer, *Nat. Mater.* **2021**, *20*, 1491.
[2] X. Y. Liang, G. D. Chen, I. M. Lei, P. Zhang, Z. Y. Wang, X. M. Chen, M. Z. Lu, J. J. Zhang, Z. B. Wang, T. L. Sun, Y. Lan, J. Liu, *Adv. Mater.* **2023**, *35*, 2207587.
[3] J. P. Jia, S. Lu, S. R. Sun, Y. J. Jin, L. G. Qin, C. Z. Zhao, *Sci. Adv.* **2025**, *11*, adr9834.
[4] Y. P. Chen, B. K. Dang, J. Z. Fu, J. Y. Zhang, H. Y. Liang, Q. F. Sun, T. Y. Zhai, H. Q. Li, *ACS Nano* **2022**, *16*, 7525.
[5] H. Zhuo, X. Y. Dong, Q. Y. Liu, L. Y. Hong, Z. L. Zhang, S. C. Long, W. Zhai, *Nat. Commun.* **2025**, *16*, 980.
[6] L. B. Mao, H. L. Gao, H. B. Yao, L. Liu, H. Cölfen, G. Liu, S. M. Chen, S. K. Li, Y. X. Yan, Y. Y. Liu, S. H. Yu, *Science* **2016**, *354*, 107.
[7] J. K. Han, G. L. Du, W. W. Gao, H. Bai, *Adv. Funct. Mater.* **2019**, *29*, 1900412.
[8] W. Huang, M. Shishehbor, N. Guarín-Zapata, N. D. Kirchhofer, J. Li, L. Cruz, T. F. Wang, S. Bhowmick, D. Stauffer, P. Manimunda, K. N. Bozhilov, R. Caldwell, P. Zavattieri, D. Kisailus, *Nat. Mater.* **2020**, *19*, 1236.
[9] R. P. Behera, H. Le Ferrand, *Matter* **2021**, *4*, 2831.
[10] L. Wang, L. Guo, K. Zhang, Y. Xia, J. Hao, X. Wang, *Angew. Chem. Int. Ed.* **2023**, *62*, 202301762.
[11] J. Lee, B. B. Jing, L. E. Porath, N. R. Sottos, C. M. Evans, *Macromolecules* **2020**, *53*, 4741.
[12] L. Peng, L. Hou, P. Y. Wu, *Adv. Mater.* **2023**, *35*, 2211342.
[13] J. H. Ni, S. T. Lin, Z. Qin, D. Veysset, X. Y. Liu, Y. C. Sun, A. J. Hsieh, R. Radovitzky, K. A. Nelson, X. H. Zhao, *Matter* **2021**, *4*, 1919.
[14] X. Y. Li, J. P. Gong, *Nat. Rev. Mater.* **2024**, *9*, 380.
[15] H. B. Wan, B. H. Wu, L. Hou, P. Y. Wu, *Adv. Mater.* **2024**, *36*, 2307290.
[16] Y. Feng, Y. Wang, C. Chen, Z. Wang, J. Liu, *Innov. Mater.* **2024**, *2*, 100105.
[17] S. M. Wen, S. M. Chen, W. T. Gao, Z. J. Zheng, J. Z. Bao, C. Cui, S. Liu, H. L. Gao, S. H. Yu, *Adv. Mater.* **2023**, *35*, 2211175.
[18] M. Y. Zhang, N. Zhao, Q. Yu, Z. Q. Liu, R. T. Qu, J. Zhang, S. J. Li, D. C. Ren, F. Berto, Z. F. Zhang, R. O. Ritchie, *Nat. Commun.* **2022**, *13*, 3247.
[19] Z. P. Xu, M. R. Wu, W. W. Gao, H. Bai, *Sci. Adv.* **2022**, *8*, abo0946.
[20] K. Haraguchi, T. Takehisa, *Adv. Mater.* **2002**, *14*, 1120.
[21] D. Yan, J. J. Luo, S. J. Wang, X. C. Han, X. D. Lei, K. Jiao, X. Q. Wu, L. Qian, X. S. Zhang, X. X. Zhao, J. T. Di, Z. Zhang, Z. F. Gao, J. Zhang, *Adv. Mater.* **2024**, *36*, 2306129.
[22] M. Kagias, S. Lee, A. C. Friedman, T. Z. Zheng, D. Veysset, A. Faraon, J. R. Greer, *Adv. Mater.* **2023**, *35*, 2209153.
[23] Z. Yin, F. Hannard, F. Barthelat, *Science* **2019**, *364*, 1260.
[24] X. Y. Liang, G. D. Chen, S. T. Lin, J. J. Zhang, L. Wang, P. Zhang, Z. Y. Wang, Z. B. Wang, Y. Lan, Q. Ge, J. Liu, *Adv. Mater.* **2021**, *33*, 2102011.
[25] J. Y. Sun, X. H. Zhao, W. R. K. Illeperuma, O. Chaudhuri, K. H. Oh, D. J. Mooney, J. J. Vlassak, Z. G. Suo, *Nature* **2012**, *489*, 133.
[26] N. Rauner, M. Meuris, M. Zoric, J. C. Tiller, *Nature* **2017**, *543*, 407.
[27] M. T. Hua, S. W. Wu, Y. F. Ma, Y. S. Zhao, Z. L. Chen, I. Frenkel, J. Strzalka, H. Zhou, X. Y. Zhu, X. M. He, *Nature* **2021**, *590*, 594.
[28] Y. H. Feng, L. J. Shan, Y. F. Wang, X. M. Chen, C. Wang, J. Liu, *ACS Nano* **2025**, *19*, 16675.
[29] G. D. Chen, X. Y. Liang, P. Zhang, S. T. Lin, C. C. Cai, Z. Y. Yu, J. Liu, *Adv. Funct. Mater.* **2022**, *32*, 2113262.
[30] J. Guo, X. D. Shu, H. Deng, J. W. Zhang, Y. Wang, G. L. Meng, J. He, F. Wu, *Acta Biomater.* **2022**, *149*, 220.
[31] D. Nepal, S. Kang, K. M. Adstedt, K. Kanhaiya, M. R. Bockstaller, L. C. Brinson, M. J. Buehler, P. V. Coveney, K. Dayal, J. A. El-Awady, L. C. Henderson, D. L. Kaplan, S. Keten, N. A. Kotov, G. C. Schatz, S. Vignolini, F. Vollrath, Y. Wang, B. I. Yakobson, V. V. Tsukruk, H. Heinz, *Nat. Mater.* **2023**, *22*, 18.
[32] J. Steck, J. Kim, Y. Kutsovsky, Z. Suo, *Nature* **2023**, *624*, 303.
[33] W. Zhao, L. J. Duan, B. Y. Zhang, X. Y. Ren, G. H. Gao, *Polymer* **2017**, *112*, 333.

[34] W. Z. Li, S. J. Zheng, X. Y. Zou, Y. Y. Ren, Z. Y. Liu, W. S. Peng, X. L. Wang, D. Liu, Z. H. Shen, Y. Hu, J. N. Guo, Z. Sun, F. Yan, *Adv. Funct. Mater.* **2022**, *32*, 2207348.
[35] H. J. Zhang, T. L. Sun, A. K. Zhang, Y. Ikura, T. Nakajima, T. Nonoyama, T. Kurokawa, O. Ito, H. Ishitobi, J. P. Gong, *Adv. Mater.* **2016**, *28*, 4884.
[36] B. O. Okesola, S. L. Ni, B. Derkus, C. C. Galeano, A. Hasan, Y. H. Wu, J. Ramis, L. Buttery, J. I. Dawson, M. D'Este, R. O. C. Oreffo, D. Eglin, H. C. Sun, A. Mata, *Adv. Funct. Mater.* **2020**, *30*, 1906205.
[37] L. J. Teng, Y. H. Chen, M. Jin, Y. G. Jia, Y. J. Wang, L. Ren, *Biomacromolecules* **2018**, *19*, 1939.
[38] X. Liang, G. Chen, S. Lin, J. Zhang, L. Wang, P. Zhang, Y. Lan, J. Liu, *Adv. Mater.* **2022**, *34*, 2107106.
[39] Y. Tan, R. X. Liao, Y. B. Mu, L. Dong, X. M. Chen, Y. Xue, Z. M. Zheng, F. C. Wang, Z. P. Ni, J. Guo, H. C. Gu, Y. F. Wang, Z. B. Wang, L. Zeng, J. Liu, *Adv. Funct. Mater.* **2024**, *34*, 2407050.
[40] D. Taylor, N. O'Mara, E. Ryan, M. Takaza, C. Simms, *J. Mech. Behav. Biomed.* **2012**, *6*, 139.
[41] S. T. Lin, X. Y. Liu, J. Liu, H. Yuk, H. C. Loh, G. A. Parada, C. Settens, J. Song, A. Masic, G. H. McKinley, X. H. Zhao, *Sci. Adv.* **2019**, *5*, aau8528.
[42] H. B. Yang, Y. X. Lu, X. Yue, Z. X. Liu, W. B. Sun, W. P. Zheng, Q. F. Guan, S. H. Yu, *Nat. Commun.* **2025**, *16*, 62.
[43] T. Hao, W. Huang, N. Guarin-Zapata, D. Lublin, Y. Chen, H. Yu, L. Shyamsunder, P. Zavattieri, D. Kisailus, *Adv. Funct. Mater.* **2025**, *35*, 2417291.
[44] Y. Y. Yang, Q. Zhou, X. K. Li, G. C. Lum, Y. Deng, *Cem. Concr. Compos.* **2019**, *104*, 103338.
[45] F. K. Shi, X. P. Wang, R. H. Guo, M. Zhong, X. M. Xie, *J. Mater. Chem. B* **2015**, *3*, 1187.
[46] Z. Y. Wu, H. Pan, P. Huang, J. H. Tang, W. She, *Adv. Mater.* **2024**, *36*, 2405183.
[47] W. Z. Li, L. L. Li, S. J. Zheng, Z. Y. Liu, X. Y. Zou, Z. Sun, J. N. Guo, F. Yan, *Adv. Mater.* **2022**, *34*, 2203049.
[48] Q. Peng, X. M. Liu, Y. G. Wei, *J. Mech. Phys. Solids* **2024**, *188*, 105680.
[49] Z. A. Jia, Y. Yu, S. Y. Hou, L. F. Wang, *J. Mech. Phys. Solids* **2019**, *125*, 178.
[50] M. Shariyat, M. Jahangiri, *Compos. Struct.* **2020**, *245*, 112345.
[51] J. Pan, Q. Peng, X. Liu, Y. Wei, *Inter. J. Solids Struct.* **2023**, *271*, 112250.
[52] B. Alheit, S. Bargmann, B. D. Reddy, *J. Mech. Phys. Solids* **2021**, *157*, 104620.